Composite Structures 268 (2021) 113925

Contents lists available at ScienceDirect

Composite Structures

journal homepage: www.elsevier.com/locate/compstruct

Tension-tension fatigue behavior of ductile adhesively-bonded FRP joints

Lulu Liu [a,b], Xin Wang [a,c,*], Zhishen Wu [a,c], Thomas Keller [b,*]

[a] Key Laboratory of C & PC Structures Ministry of Education, Southeast University, Nanjing 210096, China
[b] Composite Construction Laboratory (CCLab), École Polytechnique Fédérale de Lausanne (EPFL), Lausanne CH-1015, Switzerland
[c] National and Local Unified Engineering Research Center for Basalt Fiber Production and Application Technology, Interna- tional Institute for Urban Systems Engineering, Southeast University, Nanjing 210096, China.

ARTICLE INFO

Keywords:
FRP joints
Adhesively-bonded joints
Fatigue
Creep
Fatigue-creep interaction
Self-generated temperature
Failure displacement

ABSTRACT

The tension-tension fatigue behavior of ductile adhesively-bonded double-lap FRP joints was experimentally investigated. An acrylic adhesive, which was in the rubbery state at ambient temperature, provided the joint ductility. The fatigue degradation of the joints was characterized by the cyclic energy dissipation, cyclic stiffness, cyclic creep displacement and self-generated temperature. The effects of elevated temperature on the joints' static tensile and pure creep behaviors were also investigated. All joints failed in the adhesive layer at almost the same failure displacement, independent of the loading history (static, creep, fatigue, and temperature loading) due to the stretching of the adhesive's molecular chains until the primary bonds failed. Fatigue failure was driven by cyclic creep; the cyclic creep displacements were accelerated mainly by the damage caused by fatigue at high load levels and by the damage caused by creep and self-generated temperature at low load levels.

1. Introduction

Pultruded fiber-reinforced polymer (FRP) profiles have been the focus of increasing interest as structural members for use in new load-bearing constructions, such as FRP truss structures and FRP bridge decks, thanks to their high strength-to-weight ratio, superior chemical resistance, and low-cost transportation and construction compared to the traditional materials employed in civil engineering [1–3]. Adhesively-bonded and bolted joints are the two main techniques for connecting FRP members [3,4]. Bonded joints can provide higher stiffness, longer fatigue life, lower weight and higher compatibility with different materials than bolted joints, in which the hole drilling required may also lead to stress concentration and poor durability if exposed to environmental conditions [4–6]. Concerning bonded joints, ductile joints for use in FRP composite structures have been developed in recent years [7,8]. On the one hand, ductile adhesives can provide ductility to the joints and thus system ductility to FRP structures and thereby increase structural safety [9] and on the other hand, they enable load sharing with additional bolts in hybrid bonded-bolted joints as demonstrated in Ref. [10].

Since the live load-to-weight ratio of FRP structures is often high, particularly in the case of lightweight FRP road bridges subjected to heavy truckloads, the fatigue behaviors of such structures, and their bonded joints in particular, represent one of the most important concerns. The fatigue behavior of bonded FRP joints is mainly governed by the viscoelastic behavior of the adhesive, which (among other things) is manifested by creep effects and a loading rate and temperature dependency [11,12]. The fatigue response depends on the *R*-ratio or mean load. Increasing the fatigue mean load level (i.e. increasing the *R*-ratio) increases creep and fatigue-creep interaction effects, which may reduce fatigue life [13,14]. At the same fatigue load level, the fatigue response further depends on the frequency (i.e. loading rate). The fatigue life is basically increased with increasing frequency since the viscoelastic effects, i.e. creep and fatigue-creep interaction effects, are reduced [15,16]. Increasing the frequency may however also increase the internal friction in damaged adhesive materials and thus lead to an increase in self-generated temperature, which may then significantly reduce fatigue life [17–19]. Adapting the frequency to the load level in fatigue experiments allows a constant loading rate to be maintained and further limiting the frequency can prevent damaging self-generated temperature in the adhesive [15,19–21].

* Corresponding authors.
E-mail addresses: xinwang@seu.edu.cn (X. Wang), thomas.keller@epfl.ch (T. Keller).

https://doi.org/10.1016/j.compstruct.2021.113925
Received 20 January 2021; Accepted 28 March 2021
Available online 31 March 2021

The above effects of viscoelasticity on the fatigue life are much more pronounced in the case of ductile adhesives, such as acrylics, compared to much stiffer and brittle adhesives, such as certain epoxies [5,11,15]. Ductile adhesives may exhibit fatigue characteristics similar to those of rubber-like elastomers – the fatigue behavior of the latter materials has been widely studied and the effects of creep and internal heat generation or aspects such as energy dissipation have been thoroughly discussed [22–25].

Although a great deal of experimental and theoretical work have been carried out on the fatigue behavior of bonded FRP joints [5,11], this work, with few exceptions [17,26–28], concern adhesives that exhibit stiff and brittle behavior. The fatigue behavior of bonded FRP joints comprising a ductile adhesive, comprehensively addressing the effects of fatigue, creep, self-generated temperature and their interactions, has not yet been reported to the authors' best knowledge.

Thus, the aims of the present work were threefold: 1) to experimentally characterize the fatigue behavior of bonded FRP joints comprising a ductile adhesive, in terms of their load-fatigue life (*F-N*) curve, energy dissipation, stiffness degradation and creep displacement behaviors, 2) to derive the effects of fatigue damage, creep deformation and damage, and self-generated temperature and of their interactions concerning fatigue behavior, and 3) to provide a reference for the subsequent investigation of the fatigue behavior of hybrid joints composed of a ductile adhesive and additional steel bolts (as developed in Ref. [8]).

The work has experimentally investigated the fatigue behavior of ductile adhesively-bonded FRP double-lap joints at different load levels. The frequency was varied in order to maintain the same loading rate and thus render the results comparable. The cyclic energy dissipation, cyclic stiffness degradation, and cyclic creep were derived from the load-displacement loops measured during the fatigue cycles. Since the adhesive was highly viscoelastic, self-generated temperature could not be prevented even at very low frequencies, and the temperature was thus monitored. In addition, monotonic static tensile and pure creep experiments were performed at different temperatures to support the analysis of the fatigue-creep-temperature interactions.

2. Experimental program

The experimental program comprised four main objectives, 1) to characterize the viscoelastic behavior of the ductile adhesive through dynamic mechanical analysis (DMA); 2) to determine the effect of elevated temperatures on the monotonic tensile and pure creep behaviors of the bonded joints; 3) to derive the *F-N* curve and load-displacement responses of the individual cycles, i.e. hysteresis loops, and 4) to obtain the temperature fields of the laterally accessible adhesive surfaces.

2.1. Materials

2.1.1. BFRP adherends

Basalt-FRP (BFRP) laminates were adopted as adherends for the double-lap joints because of their excellent mechanical and superior chemical properties compared to glass-FRP (GFRP) [29,30]. BFRP plates of 4.15 mm thickness were pultruded comprising unidirectional (UD) basalt fiber rovings of 1200-tex, multidirectional (MD) basalt fabrics (0°/45°/−45°/90°) with an area density of 600 g/m^2, and an Aradur 1562-1 epoxy resin. The total fiber volume fraction was 68%, divided into 70/20/10% for the 0°/±45°/90° directions, respectively, and determined by resin burn-off experiments according to ASTM 3171 [31]. The mechanical properties of the constituent materials, provided by the manufacturer, and adherends, derived from tensile experiments according to ASTM D3039 [32], are listed in Table 1.

2.1.2. ADP adhesive

A ductile adhesive, based on Acrylic Double Performance technology [33], designated ADP in the following, was selected, which can exhibit bilinear behavior with high failure strain and energy dissipation capacity [7,10,34]. The basic mechanical properties of ADP were investigated in Ref. [35]; they exhibited significant strain-rate dependency, selected values are listed in Table 1.

DMA experiments were performed according to ASTM D7028 [36] to characterize the viscoelastic behavior of the ADP adhesive. Three specimens with dimensions of 35 × 10 × 3 mm^3 were fabricated and cured under the same conditions as the adhesively-bonded joints, i.e. for seven days under ambient laboratory conditions (T = 25 ± 5 °C, RH = 50 ± 10%). A dynamic mechanical analyzer system, DSC Q800 from TA Instruments, was used in a single cantilever configuration. The experiments were run in two cycles under a constant amplitude of 30 μm at a frequency of 1 Hz, from −120 °C to 80 °C, at a heating rate of 1.0℃/min and cooling rate of 5.0 °C/min. The resulting storage and loss moduli of the two cycles are shown in Fig. 1. They demonstrate that the adhesive can be considered almost fully cured after the curing process, since the curves of the two cycles practically overlap. The glass transition temperature (T_g) defined in structural applications as the onset value of the storage modulus decay according to [4,36], was determined from the intersection of the two tangent lines, as shown in Fig. 1. An average value of T_g = −66.1 °C, was obtained, which revealed that the adhesive was in the rubbery state at ambient temperature. At temperatures that occur due to self-heating (20–60 °C, see below and zoom in Fig. 1), the adhesive stiffness still varies considerably.

2.2. Specimen geometry and preparation

Double-lap joints were selected to minimize the effects of the load eccentricity. The adherends were cut from the pultruded BFRP plates by a water-jet machine. The dimensions of the bonded joints are shown in Fig. 2; they were consistent with those of the previous work in Ref. [10]. The tabs of the grip area and spacer plate between the two outer adherends were also cut from the BFRP plates.

The joints were fabricated in three steps: surface preparation, bonding and curing. Firstly, the adherend surfaces were abraded using an automatic sanding machine with 60-grit abrasive paper to remove release agent and surface resin until the fibers appeared at approximately 0.1-mm depth. The abraded area was then cleaned using a

Table 1
Mechanical properties of constituent materials, BFRP adherends, and ADP adhesive.

Material	Mechanical properties			
	Tensile strength (MPa)	Tensile modulus (GPa)	Failure elongation (%)	T_g (℃)
Basalt fiber rovings[a]	2100	91.0	2.30	–
Aradur 1562-1 epoxy[a]	6 ± 2.0	2.8 ± 0.25	2.65 ± 0.32	138.0
MD adherends[b]	971 ± 25	41.7 ± 1.8	2.33 ± 0.04	–
ADP adhesive[c]	12 ± 4.3	0.21 ± 0.05	59.8 ± 14.5	−66.1 ± 2.3

[a] Manufacturer data.
[b] ASTM D3039 experiments.
[c] ASTM D638 set-up, 2 mm/min displacement rate (mechanical properties).

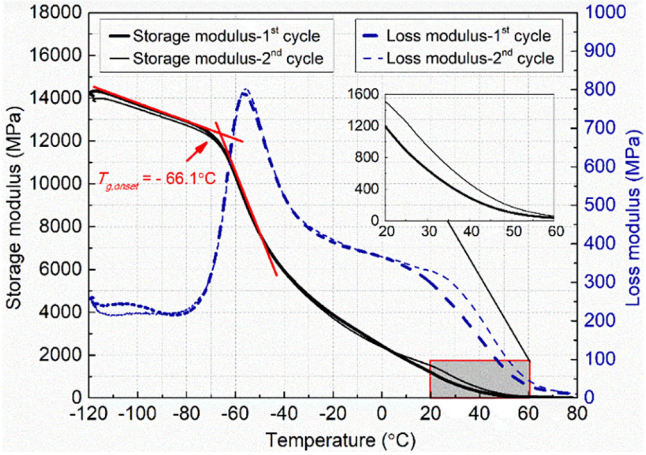

Fig. 1. Variation of storage and loss moduli of ADP adhesive from DMA experiments.

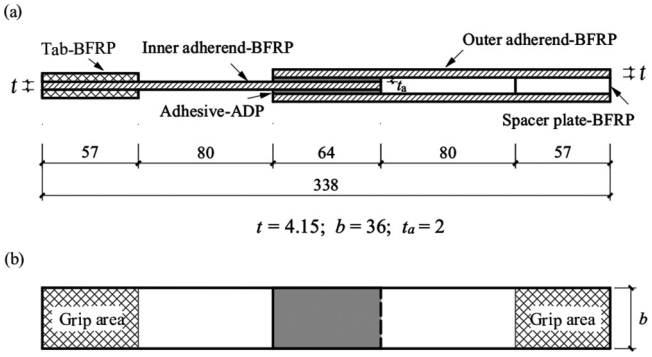

Fig. 2. Dimension of bonded joints in (mm): (a) side view; (b) top view.

cleaning and activating agent (Sika ADPrep) developed for this adhesive. Based on previous experimental experience [7,9,10], a primer, i.e. 0.1-mm-thin layer of epoxy adhesive, Sikadur 330 [37], was further applied and cured at 60 °C in an oven for four hours. The primer layer was then slightly abraded using 80-grit abrasive paper to provide a rough surface for the ADP adhesive. The alignment of the joints was assured by an in-house-developed fixture and four 2-mm-diameter glass balls were dispersed on the fresh adhesive to guarantee the target uniform adhesive layer thickness. After fabrication, weights were placed on the joints to provide pressure during the curing process. All specimens were cured as mentioned above.

2.3. Experimental set-up and instrumentation

2.3.1. Static tensile experiments

Static tensile experiments were conducted on an Instron 100 kN servo-hydraulic machine with ±0.2% load accuracy and equipped with a thermal chamber offering a temperature range from −40 to 250 °C. Six temperature levels were considered from 25 to 50 °C at 5 °C intervals, selected according to the average temperature variation in the fatigue experiments (see below). After the designated temperature value was reached, the monotonic tensile loading was applied under load control at 75.6 kN/s, which corresponded to the fatigue loading rate (see below). Furthermore, specimens were investigated at ambient temperature (24 ± 2 °C) under displacement control at 1 mm/min according to ASTM D3165 [41] (i.e. a much lower rate), and then 75.6 kN/s, to evaluate the effect of the loading rate.

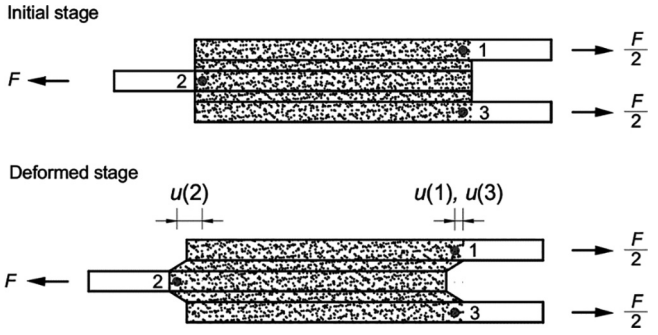

Fig. 3. Position of DIC measurement points on bonded joint at initial and deformed stages.

Type K thermocouples with wire diameter of 1.5 mm and accuracy of ±1.5 °C were embedded in the center of the adhesive layer during fabrication to measure the temperature. A thermocouple acquisition system, QuantumX MX1609, with an accuracy of ±0.1 °C, recorded the temperature at a frequency of 1 Hz. Digital image correlation (DIC) with a resolution of 2.2 Mpixels was used to measure the variation of the joint displacements via recording images at 1 Hz for specimens under displacement control and at 100 Hz under load control. An LED white light was used to enhance the contrast of the DIC painting. The joint displacements were calculated from the average values of $u(2) - u(1)$ and $u(2) - u(3)$ in the joint area, as shown in Fig. 3. The load-stroke responses were recorded by the test machine. Three specimens were investigated for each configuration, while temperatures were measured in two of them.

An overview of the static tensile experiments is given in Table 2. The specimen designation is as follows: the first term "S" indicates static experiments; the second denotes the temperature ("A" for ambient); the third indicates the loading rate, and the last one is the specimen number belonging to the same configuration.

2.3.2. Creep experiments

Creep experiments were performed according to ASTM D2990 [38] on a universal Walter + Bai 40kN test machine with ±0.5% load accuracy and equipped with a thermal chamber. Five temperature levels were considered from 30 to 50 °C at 5 °C intervals. All specimens were subjected to a constant load of 6.93 kN, which corresponded to the mean load of one configuration of the fatigue experiments ($0.23F_u$, see below). After reaching the target temperature, the specimens were loaded under displacement control at 1 mm/min up to the target load that was then maintained until creep failure occurred.

The load-stroke response and time-to-failure were recorded by the test machine at 1 Hz and DIC was employed to measure the joint displacement at selected intervals depending on the creep duration; the temperature was measured as in the static experiments. Two specimens were investigated at each temperature; an overview of the creep experiments is shown in Table 3. The designation for the specimens is as follows: the first term "C" represents creep loading; the second indicates the constant load level ($0.23F_u$); the third denotes the temperature, and the last one is the specimen number belonging to the same configuration.

2.3.3. Fatigue experiments

The fatigue experiments were performed according to ASTM D3479 [39] on the same Instron 100 kN machine as the static tensile experiments. All experiments were conducted under load control, in a sinusoidal loading waveform with constant amplitude and load ratio $R = F_{min}/F_{max} = 0.1$. Based on preliminary experiments, a constant fatigue loading rate of 75.6 kN/s, seven load levels and a maximum frequency of 5 Hz were selected. The load levels were based on the sta-

Table 2
Overview of static tensile experiments and results.

Specimen number	Specimen designation	Exposed temperature (°C)	Loading rate	Ultimate load (kN)	Failure displacement (mm)	Failure mode[a]
1	S-A-1-a	Ambient	1 mm/min	36.0	6.70	M-C-A
2	S-A-1-b			33.6	6.36	M-C-A
3	S-A-1-c			32.6	6.0	M-C-A
AV ± SD				*34.1 ± 1.75*	*5.89 ± 0.29*	
4	S-A-76-a	Ambient	75.6 kN/s	57.4	5.26	M-C-F
5	S-A-76-b			55.3	4.85	M-C-F
6	S-A-76-c			55.0	5.15	M-C-F
AV ± SD				*55.9 ± 1.08*	*5.09 ± 0.17*	
7	S-25-76-a	25	75.6 kN/s	58.1	5.35	M-C-F
8	S-25-76-b			57.2	5.12	M-C-F
AV				*57.7*	*5.24*	
9	S-30-76-a	30	75.6 kN/s	55.3	5.57	M-C-F
10	S-30-76-b			56.5	5.43	M-C-F
AV				*55.9*	*5.50*	
11	S-35-76-a	35	75.6 kN/s	53.9	5.83	M-C-F
12	S-35-76-b			54.5	6.07	M-C-F
AV				*54.2*	*5.95*	
13	S-40-76-a	40	75.6 kN/s	48.5	6.24	M-C-F
14	S-40-76-b			50.2	5.82	M-C-F
AV				*49.4*	*6.03*	
15	S-45-76-a	45	75.6 kN/s	44.6	6.43	M-C-A
16	S-45-76-b			45.1	6.52	M-C-A
AV				*44.9*	*6.48*	
17	S-50-76-a	50	75.6 kN/s	43.9	6.54	M-C-A
18	S-50-76-b			42.7	6.52	M-C-A
AV				*43.3*	*6.53*	

[a] M = mixed failure, C = cohesive, A = adhesive failure, and F = (light) fiber-tear failure.

Table 3
Overview of creep experiments and results.

Specimen number	Specimen denomination	Load level (kN)	Exposed temperature (°C)	Failure time (h)	Failure displacement (mm)	Failure mode[a]
1	C-0.23-30-a	6.93	30	733.6	6.58	M-C-A
2	C-0.23-30-b			444.7	6.63	M-C-A
AV				*589.2*	*6.61*	
3	C-0.23-35-a	6.93	35	213.1	6.92	M-C-A
4	C-0.23-35-b			207.5	6.83	M-C-A
AV				*191.2*	*6.88*	
5	C-0.23-40-a	6.93	40	34.9	6.71	M-C-A
6	C-0.23-40-b			31.7	6.95	M-C-A
AV				*34.5*	*6.83*	
7	C-0.23-45-a	6.93	45	9.1	7.02	M-C-A
8	C-0.23-45-b			11.8	7.2	M-C-A
AV				*9.3*	*7.11*	
9	C-0.23-50-a	6.93	50	3.6	7.12	M-C-A
10	C-0.23-50-b			6.0	7.25	M-C-A
AV				*4.6*	*7.19*	

[a] M = mixed failure, C = cohesive, and A = adhesive failure.

tic ultimate load, F_u (55.9 kN), obtained at the same loading rate, and selected from 8.4 to 29.5 kN (i.e. $0.15F_u$, $0.19F_u$, $0.23F_u$, $0.26F_u$, $0.30F_u$, $0.38F_u$, $0.53F_u$) to cover fatigue lives from 10^2 to $2{\cdot}10^6$ cycles.

The preliminary experiments also showed that even at a very low frequency, small but, in view of the sensitivity of the adhesive, significant temperature increases occurred in the adhesive layer, mainly towards the end of the fatigue life. Since temperature increases could not be prevented, the maximum frequency selected was 5 Hz, as also suggested in Ref. [40], and also to be able to perform the experiments within a reasonable time frame. To keep the loading rate constant, the frequency was then adapted to the load level according to the relationship between frequency, f, load amplitude, F_a, and loading rate, $\dot{F}$, i.e. $\dot{F} = 4F_a f$ [20], resulting in frequencies from 1.4 to 5.0 Hz.

The fatigue loading was applied in three steps, as shown in Fig. 4. Firstly, a monotonic tensile load was applied up to the mean load level under load control at 2 kN/s, followed secondly by a transition loading during 10 s with increasing load amplitude until the desired peak and valley loads were approached, and thirdly, the targeted fatigue loading was applied until failure or up to 2 million cycles. Specimens exceeding 2 million cycles were considered as run-out and monotonic tensile loading was subsequently applied up to failure, under displacement control at 1 mm/min.

Different instrumentation was used to monitor the mechanical and thermal properties during the cyclic loading. The load-stroke responses and number of cycles were recorded by the Instron machine. DIC was used to measure the variation of the joint displacements by

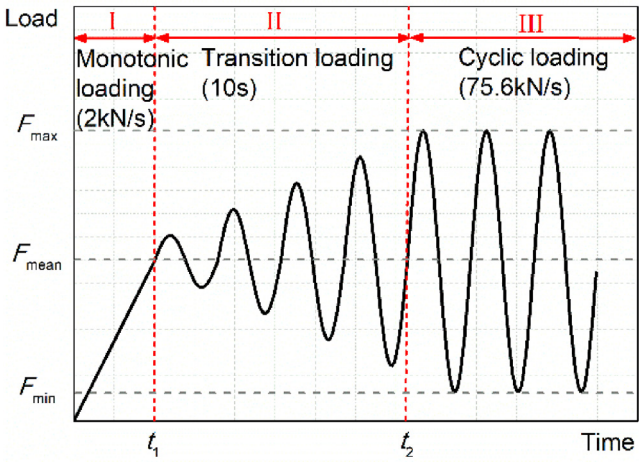

Fig. 4. Loading procedure for fatigue experiments.

recording images at 100 Hz for specified cycle intervals. The evolution of the self-generated temperature on the lateral specimen surfaces, where the adhesive layers were accessible, was monitored at 0.01 Hz for $0.15F_u$, 0.1 Hz from 0.19 to $0.38F_u$, and 1 Hz for $0.53F_u$, using an infrared (IR) thermal camera with an accuracy of ±0.1 °C, at an optical resolution of 160 × 120 pixels. A QuantumX MX1609 device connected to a thermocouple was used to measure the change of the ambient temperature around the Instron machine during the fatigue loading with a frequency of 0.02 Hz.

Three specimens were examined at each selected load level and all fatigue experiments were performed in the same air-conditioned laboratory environment (T = 24 ± 2 °C, RH = 45 ± 5%) to minimize the effects of ambient temperature changes. An overview of the fatigue experiments is given in Table 4. The designation of the specimens is as follows: the first term "F" indicates fatigue loading; the second denotes the load level, and the third is the specimen number belonging to the same configuration.

3. Experimental results and discussion

3.1. Static tensile behavior

3.1.1. Static tensile behavior under different loading rates

Representative load-displacement responses of the bonded joints under the two different loading rates are shown in Fig. 5. The bonded joints exhibited an approximately bilinear and highly rate-dependent behavior; a slight hardening was observed at the lower rate prior to failure, which was attributed to a stretching of the adhesive's molecular chains. The yield and ultimate (maximum) loads increased with increasing loading rate, although with slightly decreasing failure displacements in the latter case. The ultimate loads and failure displacements are also listed in Table 2.

The failure mode at the low rate was a mixed cohesive/adhesive failure (according to ASTM 5573 [41]), designated M-C-A, as shown in Fig. 6(a) and Table 2. It changed to mixed cohesive/(light) fiber-tear failure at the high rate, designated M-C-F, as shown in Fig. 6(b).

3.1.2. Static tensile behavior at different temperatures

The typical load-displacement responses of the bonded joints at the different temperatures from 25 °C to 50 °C, under load control at 75.6 kN/s, are shown in Fig. 7. The elastic stiffness, yield and ultimate loads decreased with increasing temperature, while the failure displacements showed only a slight increase, which was attributed to the thermal expansion of the joints. The slope of the post-yield

Table 4
Overview of fatigue experiments and results.

Specimen number	Specimen denomination	Load level	F_{max} (kN)	F_{min} (kN)	F_{mean} (kN)	F_a (kN)	f (Hz)	N_f (–)	Failure displacement (mm)	Failure mode[a]
1	F-0.53-a	0.53	29.50	2.95	16.21	13.26	1.4	287	5.88	M-C-F
2	F-0.53-b	0.53						246	5.69	M-C-F
3	F-0.53-c	0.53						230	6.25	M-C-A
AV ± SD								*254 ± 29*	*5.94 ± 0.28*	
4	F-0.38-a	0.38	21.05	2.11	11.58	9.47	2.0	1,843	5.86	M-C-A
5	F-0.38-b	0.38						1,356	5.54	M-C-A
6	F-0.38-c	0.38						2,199	6.58	M-C-A
AV ± SD								*1,799 ± 423*	*5.99 ± 0.54*	
7	F-0.30-a	0.30	16.80	1.68	9.24	7.56	2.5	6,994	7.80	M-C-A
8	F-0.30-b	0.30						7,734	6.51	M-C-A
9	F-0.30-c	0.30						4,071	7.54	M-C-A
AV ± SD								*6,266 ± 1937*	*7.28 ± 0.68*	
10	F-0.26-a	0.26	14.74	1.47	8.10	6.64	2.9	9,496	7.26	M-C-A
11	F-0.26-b	0.26						12,968	7.54	M-C-A
12	F-0.26-c	0.26						14,049	7.26	M-C-A
AV ± SD								*12,171 ± 2 379*	*7.35 ± 0.16*	
13	F-0.23-a	0.23	12.60	1.26	6.93	5.67	3.3	43,872	7.74	M-C-A
14	F-0.23-b	0.23						54,035	7.86	M-C-A
15	F-0.23-c	0.23						45,186	7.34	M-C-A
AV ± SD								*47,698 ± 5527*	*7.64 ± 0.27*	
16	F-0.19-a	0.19	10.53	1.53	6.03	4.50	4.2	696,712	7.90	M-C-A
17	F-0.19-b	0.19						777,559	7.51	M-C-A
18	F-0.19-c	0.19						700,912	7.89	M-C-A
AV ± SD								*725,061 ± 45,513*	*7.77 ± 0.22*	
19	F-0.15-a	0.15	8.40	0.84	4.62	3.78	5.0	>2,000,000	–	–
20	F-0.15-b	0.15						1,424,720	8.09	M-C-A
21	F-0.15-c	0.15						1,809,640	7.92	M-C-A
AV ± SD								–	–	–

[a] M = mixed failure, C = cohesive, A = adhesive failure, and F = (light) fiber-tear failure.

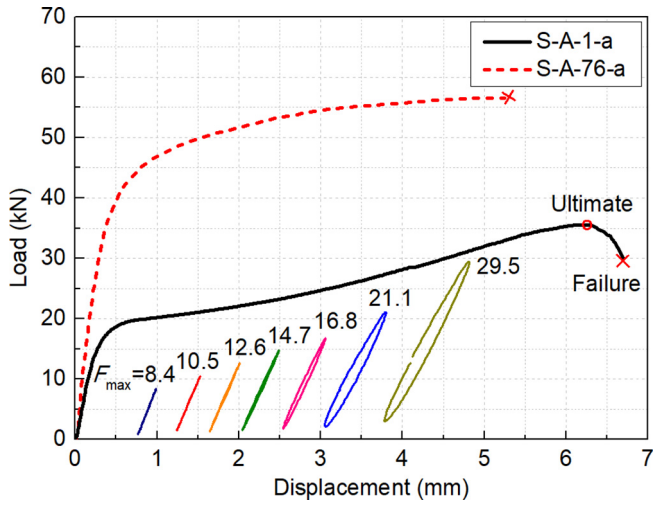

Fig. 5. Static tensile load-displacement curves at different loading rates and typical fatigue loops at different load levels.

responses did not significantly change until failure was approached, since a similar molecular stretching process occurred in the adhesive layer. Prior to failure, the stiffness slightly decreased, which was attributed to damage formation.

The decrease of the elastic joint stiffness that occurred with increasing temperature exhibited an almost linear relationship with the corresponding decrease of the DMA storage modulus of the adhesive (Fig. 1), as shown in Fig. 8; the values were normalized by the 25 °C values, taking the average in the case of the joints. They did not fully match the equality line ($y = x$), since they were obtained from two different types of experiments, exhibiting different types of stiffness.

The ultimate load depended almost linearly on the temperature, as shown in Fig. 9, and decreased by approximately 25% when the temperature increased from 25 to 50 °C, see Table 2. It should be noted that the average value of the ultimate load obtained at ambient temperature under the same displacement control of 1 mm/min (34.1 kN) was 17% lower than that in Ref. [10]; this difference was attributed to the change in seasonal temperature (12 ± 5 °C in Ref. [10], the laboratory not being air-conditioned in the latter case).

The temperature variation obtained from the thermocouples inside the adhesive layers during heating to the different target temperatures and during subsequent loading (at constant target temperatures) until ultimate failure is shown in Fig. 10. A significant temperature increase was observed as failure approached, as is also shown in Fig. 11, where the temperature increase on the two lateral adhesive edges of a specimen loaded at 25 °C is shown. The temperature slightly increased from 25 to 30 °C on average during the post-yield loading (see joint displacements in Fig. 7), and then suddenly increased up to a maximum of 54.2 °C at failure, i.e. the temperature more than doubled. This temperature increase was attributed to dissipated energy through friction caused by the increasing damage prior to failure (which also caused the stiffness decrease mentioned above).

The failure mode changed from mixed cohesive/(light) fiber-tear (M-C-F) at lower temperatures to mixed cohesive/adhesive (M-C-A) when the temperatures were above 40 °C, as shown in Fig. 12 and Table 2.

3.2. Creep behavior at different temperatures

Representative total displacement responses versus the normalized creep-time are shown in Fig. 13, at different temperatures ranging from 30 to 50 °C. The curves revealed the typical three creep stages: the primary stage, at which the displacements increased rapidly but at a decreasing rate; they subsequently entered the secondary steady stage, and then rapidly increased up to failure in the tertiary stage. The secondary stage dominated for approximately 75% of the total creep time; the slope of the curves was almost independent of temperature at this stage in the normalized form.

The total displacements are listed in Table 3 and were defined at the onset of the tertiary stage, as suggested by ASTM D2990-17 [38], since the ductile adhesive did not exhibit an abrupt failure (see below). They did not significantly vary and are composed of the initial (instantaneous) displacements and creep displacements; if the former increased with increasing temperature, the latter decreased accordingly. In contrast to the total displacements, the creep failure time, t_f, significantly decreased with increasing temperature, as shown in Fig. 14 and listed in Table 3. The relationship between creep failure time, on a logarithmic scale, and temperature was linear. The failure modes are shown in Fig. 15; the specimens consistently exhibited mixed cohesive/adhesive failure (M-C-A), where cohesive failure dominated.

3.3. Fatigue behavior

3.3.1. Fatigue life

The variation of the fatigue maximum load, F_{max}, against fatigue life (number of cycles to failure), N_f, on a logarithmic scale, is shown in Fig. 16; a classic power law relationship, expressed by Eq. (1), was used to fit the *F-N* experimental data:

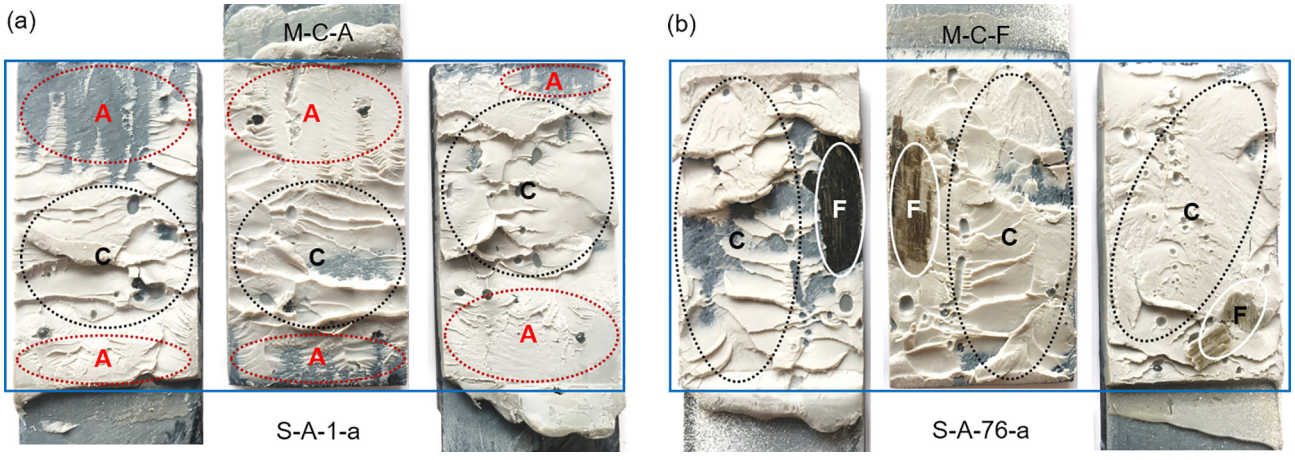

Fig. 6. Static failure modes at different loading rates: (a) 1 mm/min; (b) 75.6 kN/s (A = adhesive/interface, C = cohesive in adhesive, F = (light) fiber-tear failure).

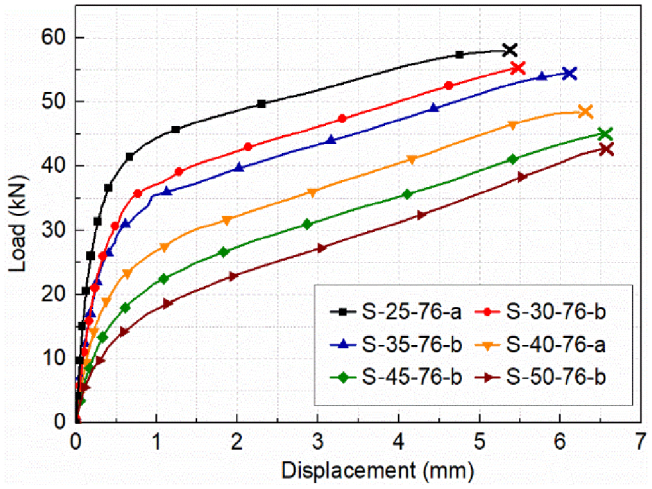

Fig. 7. Load-displacement responses for bonded joints at different temperatures.

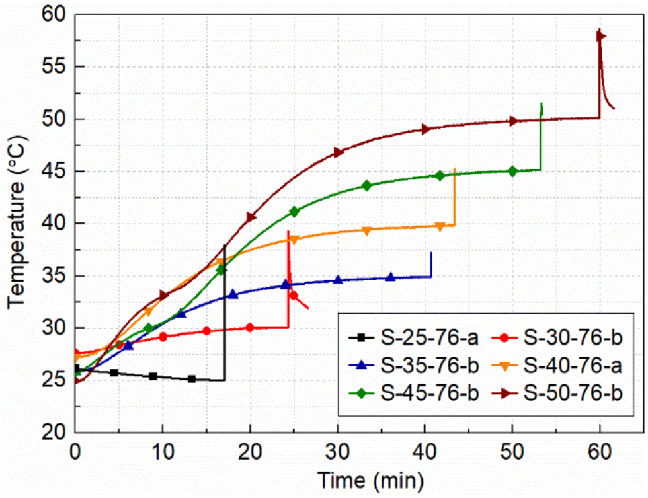

Fig. 10. Temperature variation inside adhesive layer during heating process and subsequent loading until failure.

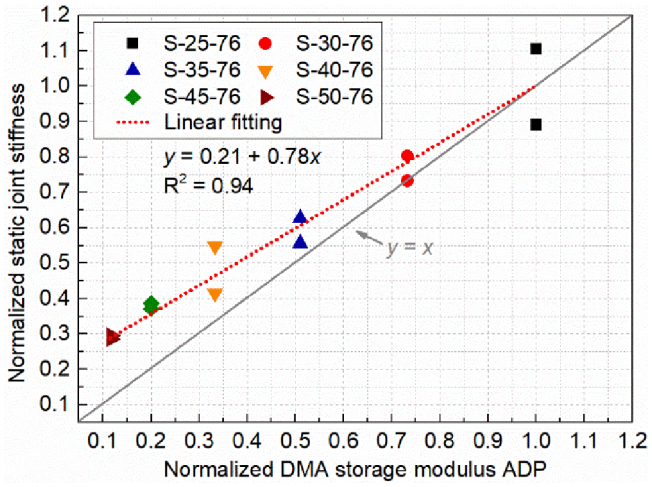

Fig. 8. Static elastic joint stiffness versus adhesive DMA storage modulus in 25–50 °C range.

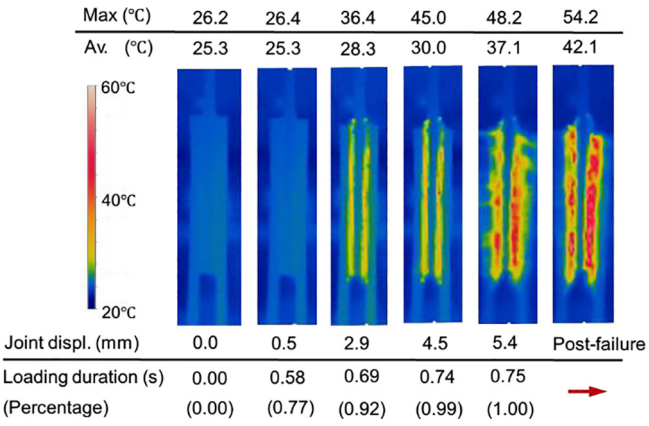

Fig. 11. Temperature variation on lateral specimen side during loading at 25 °C (joint displacement see Fig. 7).

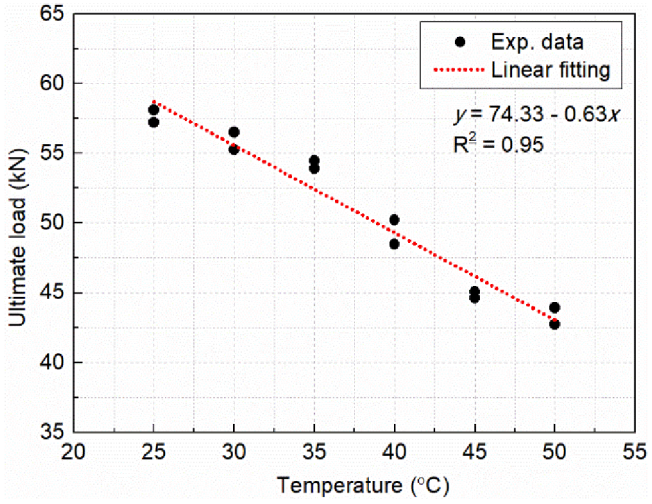

Fig. 9. Ultimate load versus temperature and linear fitting.

$$F_{\max} = F_0 N_f^{-k} \tag{1}$$

where F_0 and k are the model parameters obtained from the regression analysis, i.e. $F_0 = 56.32$ kN and $k = 0.13$.

Only one specimen survived the 2 million cycles (F-0.15-a); this run-out specimen is indicated with a right-facing arrow in Fig. 16 and was not included in the regression analysis.

The post-fatigue static tensile behavior of the run-out specimen is shown in Fig. 17 and compared to a specimen of the static experimental series (S-A-1-a), both under 1 mm/min displacement control. No obvious ultimate load decrease was observed, only a slight decrease of the failure displacement and degradation of the elastic stiffness, k, occurred due to the preceding fatigue loading.

3.3.2. Load-displacement loops

Typical load-displacement hysteresis loops up to failure are shown in Fig. 18 for a medium load level of $0.23F_u$ (12.6 kN) and high load level of $0.53F_u$ (29.5 kN). As shown in Fig. 5, the fatigue cycles were located in the ascending linear branch of the static load-displacement curve. These results can be characterized as schematically shown in Fig. 19, in terms of cyclic energy dissipation, cyclic stiffness degradation, and cyclic creep displacements [20,42], where $N = 1$ indicates the first cycle and $N = f$ the cycle at failure.

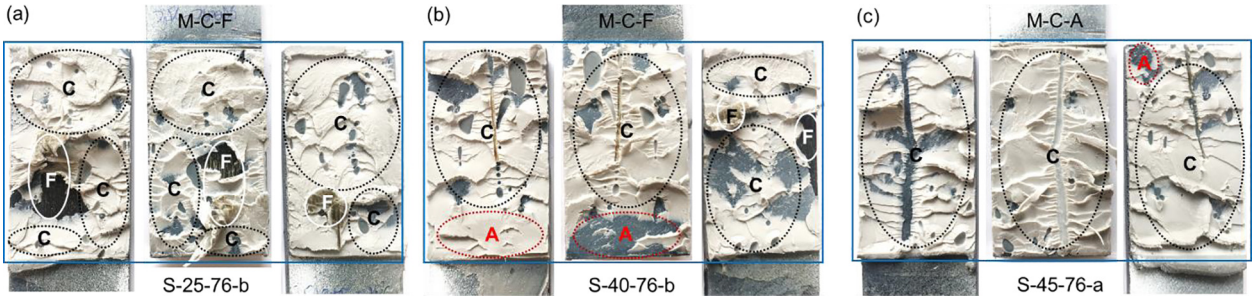

Fig. 12. Static failure modes at different temperatures: (a) 25 °C; (b) 40 °C and (c) 45 °C (A = adhesive/interface, C = cohesive in adhesive, F = (light) fiber-tear failure).

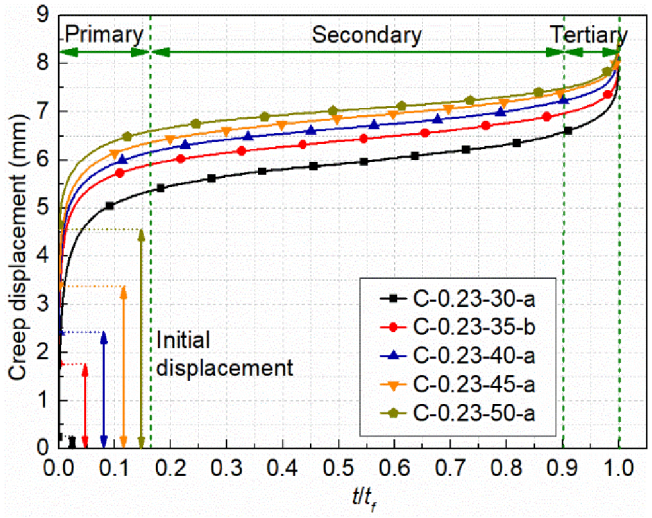

Fig. 13. Creep displacements versus normalized creep time at different temperatures.

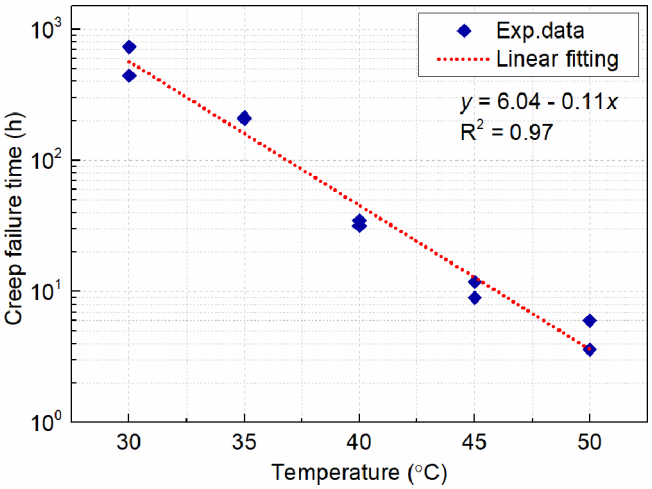

Fig. 14. Variation of creep failure time versus temperature.

The cyclic energy dissipation is represented by the hysteresis area, A_N, which includes the energies dissipated by damage (rupture of primary bonds and microcrack formation), viscoelastic deformation (debonding/rebonding of secondary bonds and intermolecular friction), and the self-generated heat (through friction in microcracks), which increased temperature.

The cyclic stiffness is a short-term stiffness, indicated by the slope of the loop, E_N, and is affected by damage formation due to fatigue and creep and self-generated temperature; it can also be increased by molecular stretching effects.

The cyclic creep displacement is represented by the shift of the loop, $d_{N,av} - d_{1,av}$, and depends on viscoelastic deformation, damage formation due to fatigue and creep, and self-generated temperature, where damage formation and self-generated temperature may affect the viscoelastic properties and accelerate the creep deformation.

These three characteristics will be analyzed in the following sections. In Fig. 18, it can already be seen that, in both cases, significant energy was dissipated towards failure. At the high load level, the loops were no longer closed since the displacements could not fully recover during unloading. The cyclic stiffness was reduced in both cases as failure approached. However, at the low load level, a small cyclic stiffening was observed during the last cycles ("banana shape" of the loops [43]), which was attributed to the stretching of the adhesive's molecular chains, as mentioned above. Cyclic creep deformations occurred from the beginning and increased throughout the whole fatigue life in both cases.

3.3.3. Energy dissipation

The relationship between cyclic energy dissipation and normalized number of cycles is shown in Fig. 20, at the different load levels. Basically, more energy was dissipated by cycle with increasing cycle number and load level. The variation of energy dissipation could be characterized by three stages. The first stage was very short and could be clearly seen only at the highest load level where the dissipated energy rapidly increased. At the second stage, the dissipated energy then continually increased, but at a low rate, up to 80–90% of the whole fatigue life. During the third stage, the energy dissipation increased exponentially until fatigue failure. The rate at the second stage was dependent on the load level; higher load levels led to higher rates; at the lowest load levels, energy dissipation was not significant.

The total dissipated energy (TDE), defined as the summation of the hysteresis areas per cycle, versus the maximum fatigue load, is shown in Fig. 21, in a semi-logarithmic plot, and fitted by a power law function. The results revealed that the TDE exponentially increased as the maximum load decreased. Although much less energy was dissipated per cycle at lower load levels, the summation during the much longer fatigue life resulted in higher amounts of TDE. The relationship between TDE and fatigue life was linear in a logarithmic plot, as shown in Fig. 22; a similar result was obtained in Ref. [20] for matrix-dominated FRP laminates.

3.3.4. Cyclic stiffness

The normalized cyclic stiffness versus the normalized number of cycles, at different load levels, is shown in Fig. 23. The stiffness degradation followed the typical three stages. During the first stage, a significant stiffness decrease could be observed, however only for the low

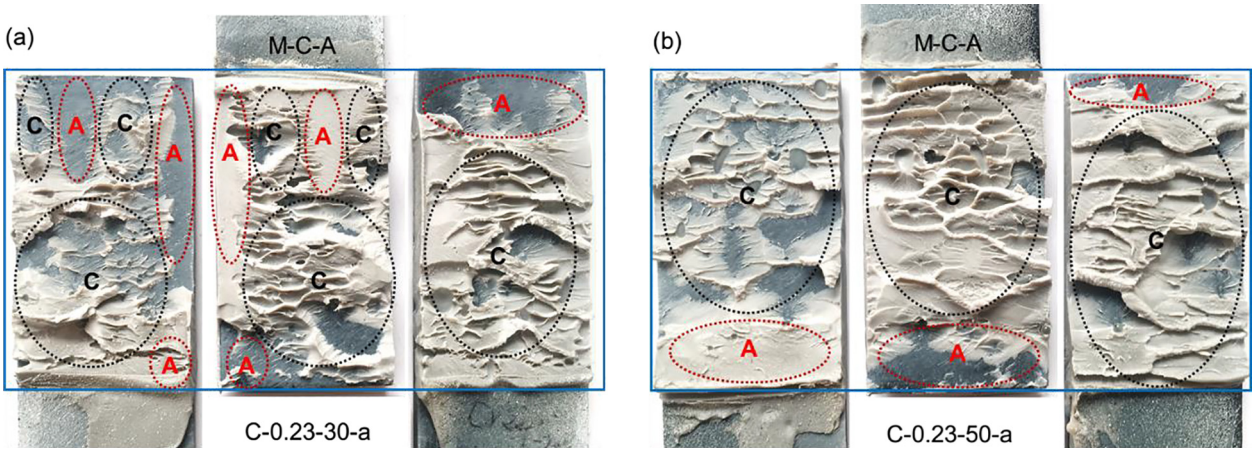

Fig. 15. Creep failure modes at different temperatures: (a) 30 °C and (b) 50 °C (A = adhesive/interface, C = cohesive in adhesive).

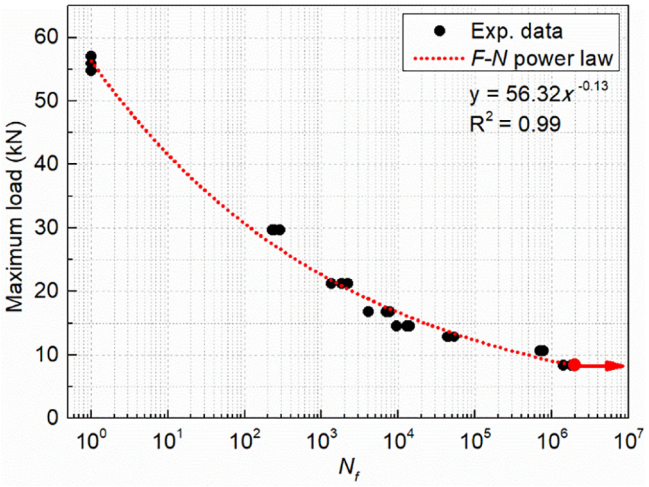

Fig. 16. Experimental fatigue data and fitted *F-N* curve.

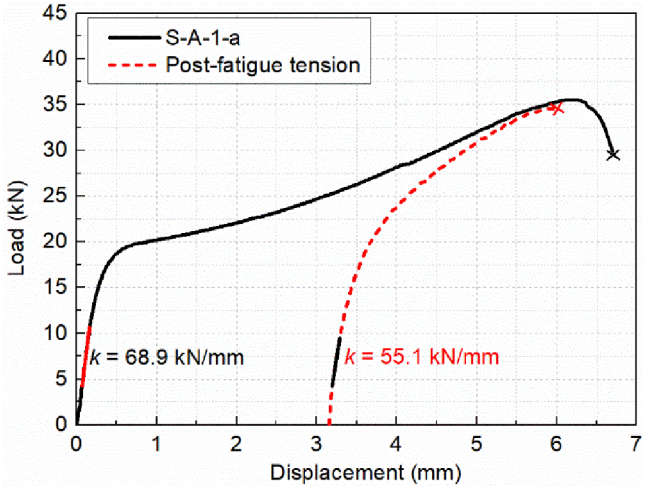

Fig. 17. Post-fatigue tensile behavior compared to behavior without preceding fatigue.

load levels, the higher levels did not clearly exhibit this stage. Subsequently, during the second stage, the stiffness remained almost unchanged at the lower load levels, while a slight decrease was observed at the higher levels up to 80–90% of the whole fatigue life. At the third stage, the stiffness exhibited a rapid decrease until ultimate failure. The stiffness at failure varied from around 67% at the highest to only around 16% at the lowest load level.

3.3.5. Cyclic creep displacements

The cyclic creep displacements versus the normalized number of cycles, at different load levels, are shown in Fig. 24. Again, a three-stage behavior was observed. During the first stage, the displacements at the lower load levels increased rapidly; the rates then decreased during the second stage until 80–90% of the fatigue life was reached. At medium load levels, the first stage did not occur, the displacements continuously increased up to the end of the second stage. At the highest load level, however, the first stage was again exhibited, i.e. the displacements increased at a higher rate than in the second stage. During the third stage, all the displacements exponentially increased up to failure. The displacements at failure varied from around 5.8 mm at the highest to 8.0 mm at the lowest load level.

3.3.6. Failure modes

The specimens subjected to fatigue loading exhibited a mixed cohesive/adhesive failure (M-C-A), with the exception of two specimens at the highest load level, which exhibited a mixed cohesive/(light) fiber-tear failure (M-C-F), see Fig. 25 and Table 4.

3.3.7. Self-generated temperature

The fatigue experiments were performed in an air-conditioned room at a temperature of 24 ± 2 °C. Nevertheless, the temperature around the test machine was monitored during the fatigue experiments since the adhesive was sensitive to small temperature changes (see above). As shown in Fig. 26, only smaller temperature fluctuations were measured around the machine, which were not regarded as significant since the fatigue results were consistent throughout, i.e. the fatigue lives for the same configuration, for instance, exhibited only small amount of scatter, as listed in Table 4.

The average temperatures measured on the lateral surfaces, at the different load levels, versus the normalized number of cycles, are shown in Fig. 27; once more a three-stage behavior was exhibited. During the first stage, the temperatures increased rapidly at lower load levels – the higher levels did not show this effect. At the second stage, the temperatures at low load levels remained almost constant, while they continuously increased at higher levels, up to 80–90% of the fatigue life. During the third stage, all temperatures exponentially increased up to failure. The temperatures close to or at failure were higher at lower than at higher load levels; however, the results were

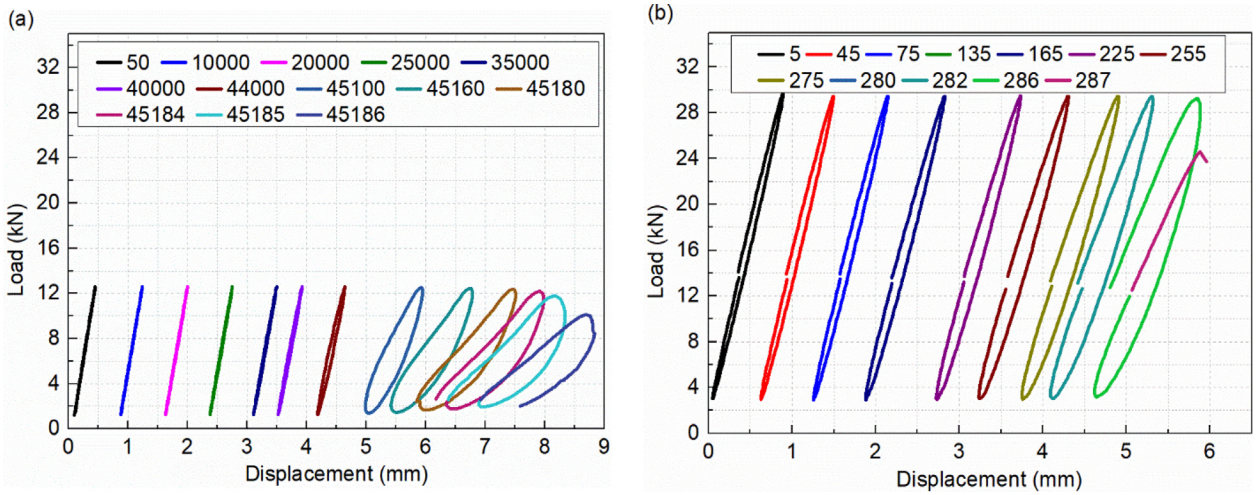

Fig. 18. Variation of hysteresis loops at indicated number of cycles for (a) F-0.23-a (F_{max} = 12.6 kN) and (b) F-0.53-a (F_{max} = 29.5 kN).

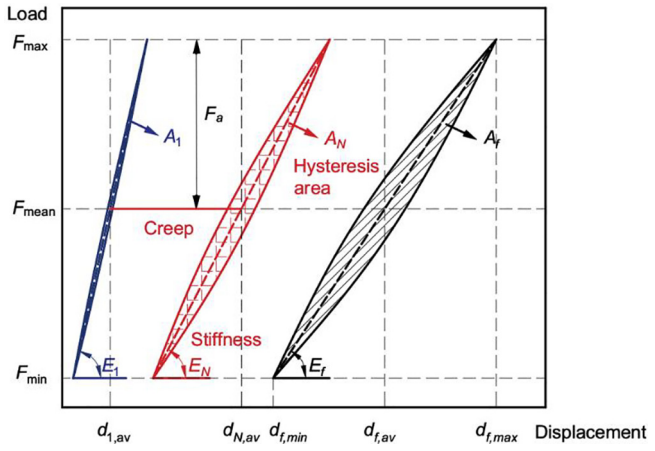

Fig. 19. Definitions for cyclic energy dissipation, cyclic stiffness, and cyclic creep displacement.

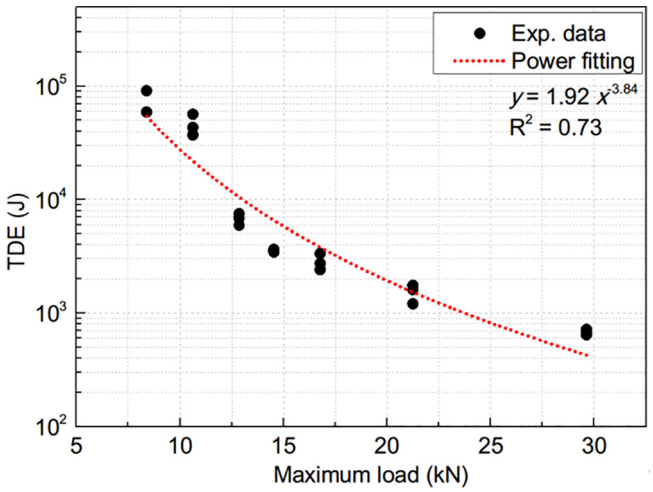

Fig. 21. Total dissipated energy (TDE) versus maximum fatigue load.

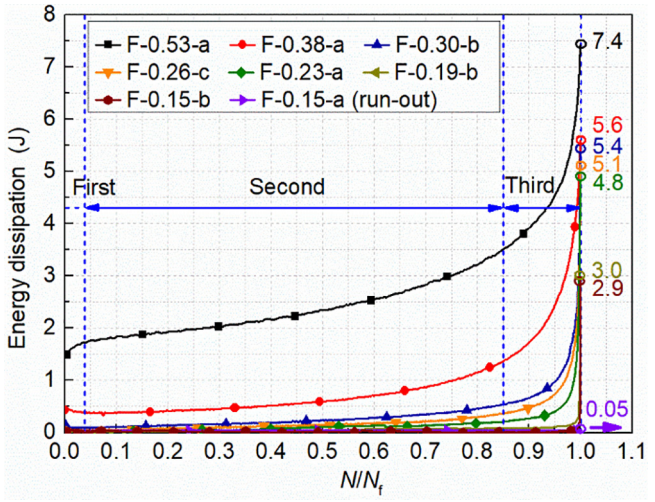

Fig. 20. Energy dissipation per cycle versus normalized number of cycles at different load levels.

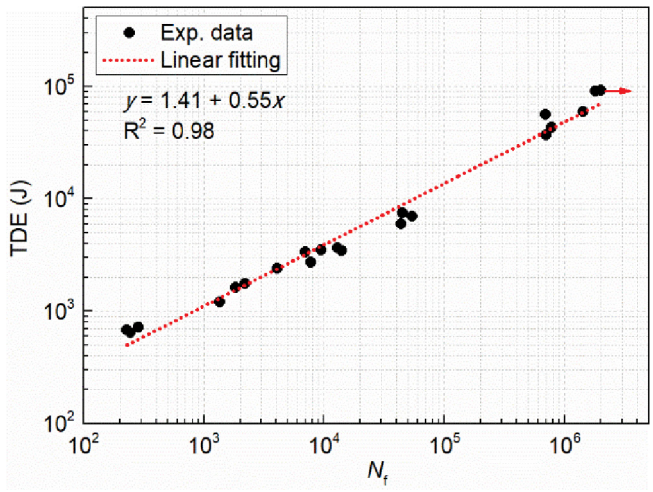

Fig. 22. Total dissipated energy (TDE) versus fatigue life at different load levels.

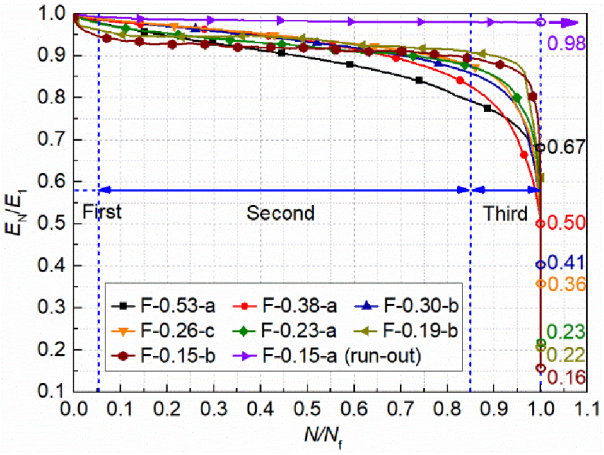

Fig. 23. Normalized fatigue stiffness versus normalized number of cycles at different load levels.

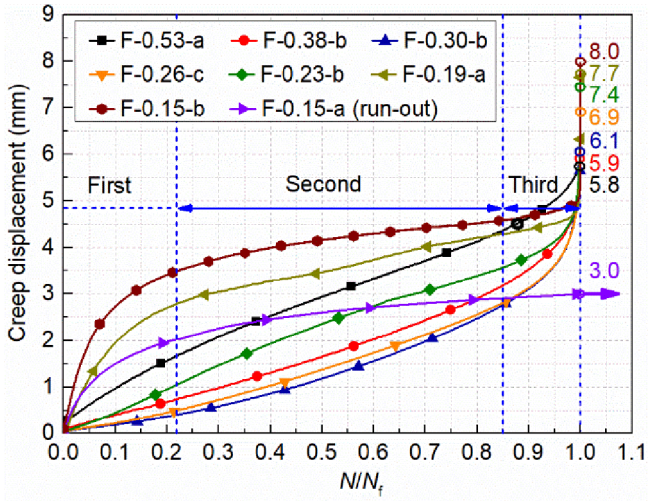

Fig. 24. Creep displacement versus normalized number of cycles at different load levels.

not fully consistent due to a limited recording frequency at low load levels.

Typical self-generated temperature distributions and magnitudes measured on the lateral joint surfaces, at different percentages of fatigue life, are shown in Fig. 28 for two load levels. The initiation and propagation of the hotspots were directly related to the damage formation and growth. During the first approximately 75% of the fatigue life,

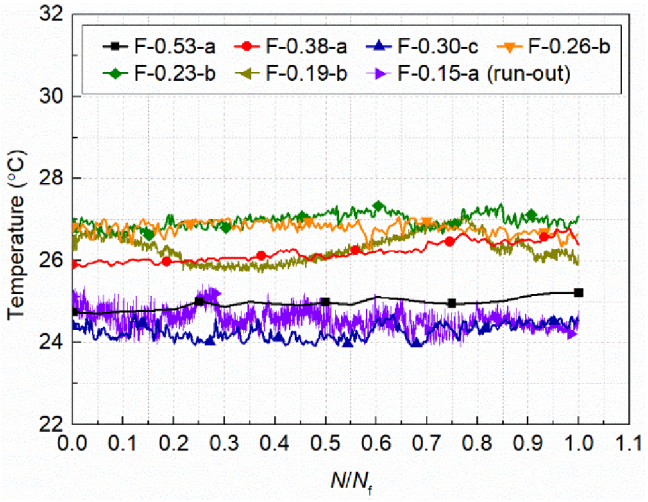

Fig. 26. Ambient temperature versus normalized number of cycles around test machine.

the hotspots developed at the top in both specimens, i.e. on the side of the tensile (peel) stresses, where damage initiated – exhibiting however only moderate temperature increases, limited to less than 35 °C on average. Subsequently, adhesive failure (debonding) initiated at these locations in both specimens, see Fig. 25 (marked "A"). In specimen F-0.19-a (Fig. 28(a)), the hotspot propagated to the middle area, consistent with the debonding on one side, which propagated significantly towards the middle of the overlap, see Fig. 25(a). In specimen F-0.26-a (Fig. 28(b)), however, the propagation of the hotspot towards the middle was much less, the temperatures developed over the whole overlap length, again in accordance with the much smaller propagation of the debonding, see Fig. 25(b). The uniform temperature distribution indicated that damage formation and progression occurred evenly distributed over the whole adhesive layer. The final hotspots were always located in regions exhibiting subsequent cohesive failure in the adhesive, i.e. in regions where most of the energy was dissipated; the temperatures therefore increased considerably up to an absolute peak value of 71.4 °C.

4. Fatigue-creep-temperature interaction

4.1. Failure displacement versus loading history

It was observed that all specimens failed at similar failure displacements, regardless of the loading history, i.e. static tension under different rates and temperatures, creep under different temperatures, or fatigue at different load levels, see Fig. 29. This may be attributed to

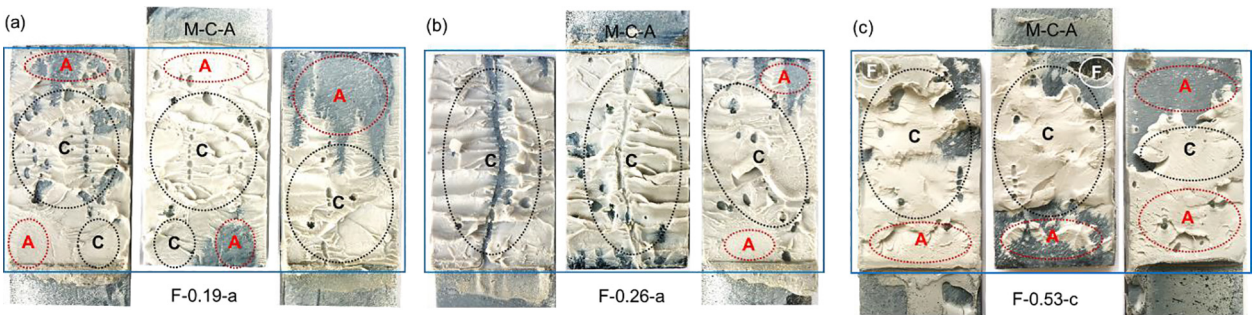

Fig. 25. Fatigue failure modes for fatigue load of (a) F-0.19-a (10.53 kN), (b) F-0.26-a (14.74 kN), and (c) F-0.53-c (29.50 kN) (A = adhesive/interface, C = cohesive in adhesive, F = (light) fiber-tear failure).

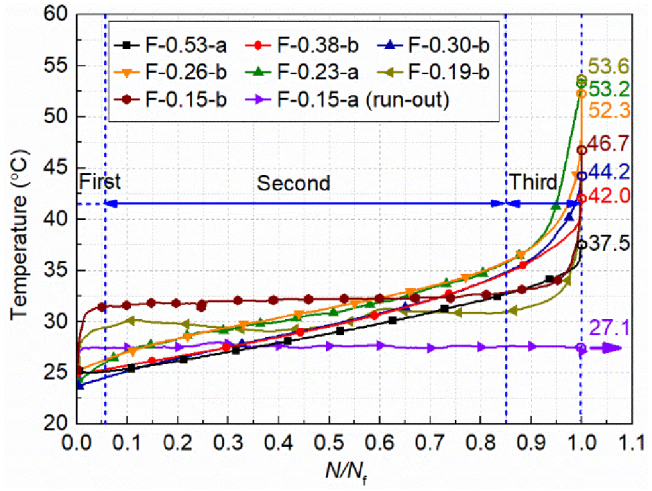

Fig. 27. Average temperature versus normalized number of cycles at different load levels.

the fact that the adhesive molecule chains were fully stretched at failure, in almost all cases, i.e. failure always occurred when the primary bonds of the stretched molecule chains failed. This stretching of the chains occurred as a result of their increased mobility caused by 1) the loss of the secondary bonds, either by yielding, creep or temperature, or 2) damage, caused by fatigue or creep. This hypothesis is supported by the failure modes; in the areas of cohesive failure, "remnants" of tension ties can be seen in cases of supposed full stretching, see Fig. 30. These failure modes were independent of the load history.

The lowest failure displacements were obtained at high rate and low temperature (static experiments) and the high load level in the fatigue experiments – thus in cases where mobility was lower and the molecule chains could not stretch fully. Furthermore, full stretching was generally prevented in the static experiments under load control, and the additional stretching during softening, observed under displacement control and shown in Fig. 5, could not be exploited. According to the established hypothesis, in cases of full molecular stretching, failure would thus always occur at a similar strain, i.e. at the strain where the primary bonds of the stretched molecules fail, independent of the loading history. Based on this hypothesis, a strain failure criterion could be established, but much more research is needed in order to do so.

4.2. Fatigue-creep interaction

The creep displacements of creep experiment C-0.23-30-a and fatigue experiment F-0.23-a are compared in Fig. 31. Both experiments were conducted at 6.93 kN (mean load in the fatigue case) and at 30 °C (average temperature during the second stage in the fatigue case, see Fig. 27), and both specimens failed at a similar failure displacement. The results show that this displacement was reached much more rapidly in the fatigue than in the creep experiment. The creep rate in the fatigue experiment was thus much higher, which can be attributed to an alteration of the viscoelastic properties caused by damage due to fatigue.

Concerning Fig. 24, the different first-stage behavior of the creep displacements can be attributed to the prevalence of either creep or fatigue effects. At low load levels, creep deformations were dominant and the displacements increased rapidly, fatigue damage did not yet occur (see also low energy dissipation in Figs. 18(a) and 20). At the medium load levels, the displacements were small and creep deformations and fatigue damage were not significant. At the high load level, however, early damage due to fatigue occurred (see high energy dissipation in Fig. 20), which accelerated creep significantly and resulted in notable creep effects in the first stage, although the life was short. At the third stage, creep entered the tertiary stage at low load levels and creep damage occurred, which was greater than the fatigue damage. At

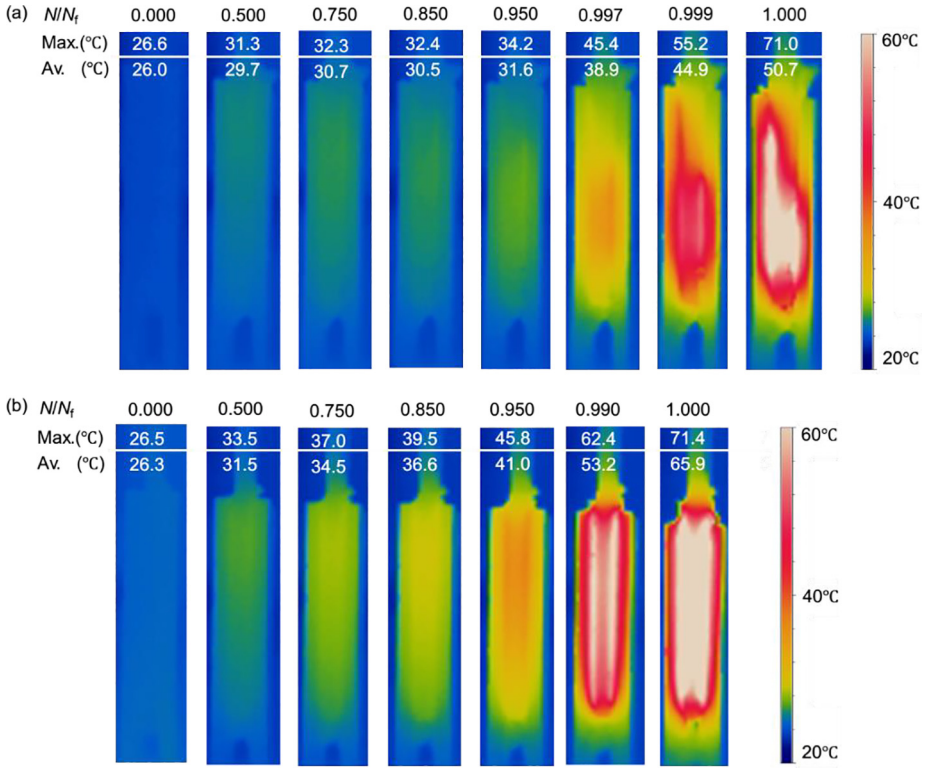

Fig. 28. Self-generated temperature distributions at different percentages of fatigue life of load level of (a) F-0.19-a (10.53 kN) and (b) F-0.26-a (14.74 kN).

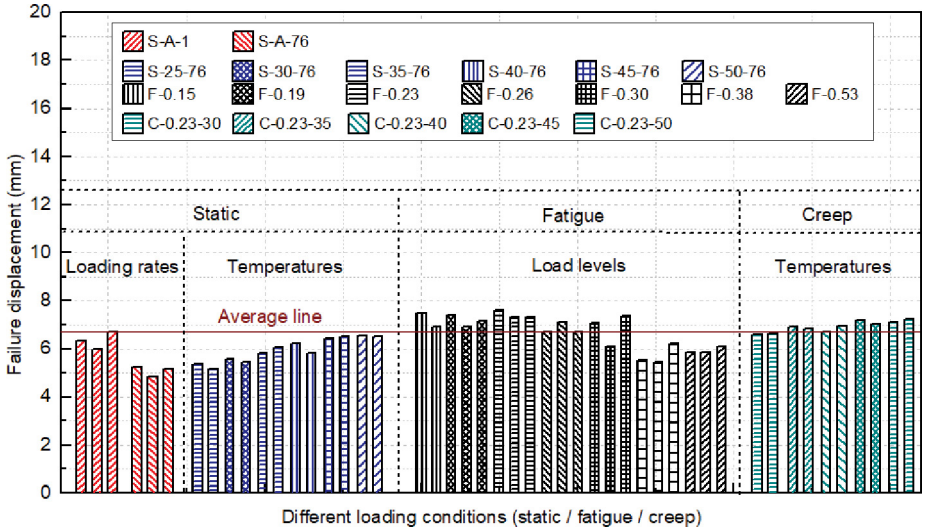

Fig. 29. Failure displacements from static, creep and fatigue experiments.

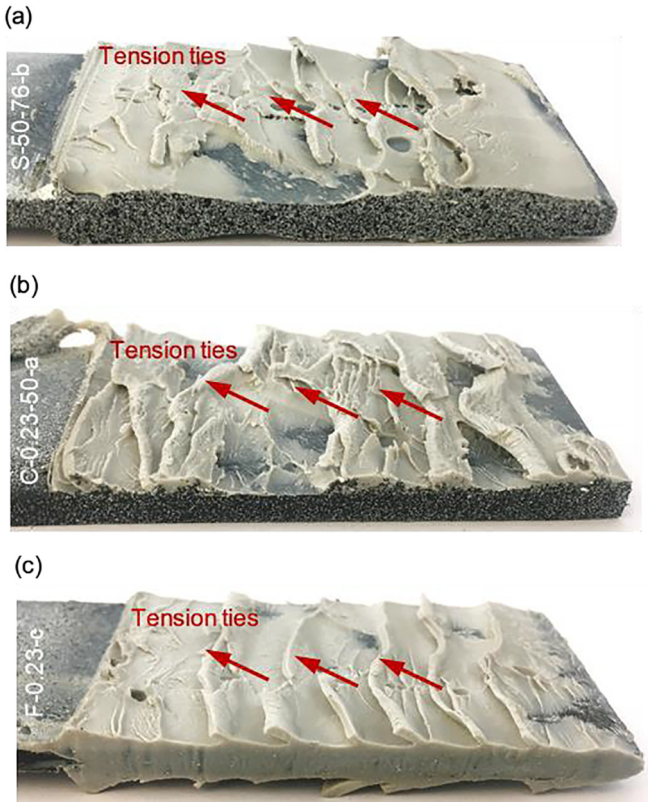

Fig. 30. Similar failure modes and remnants of tension ties in cohesive failure zones, (a) static S-50-76-b, (b) creep C-0.23-50-a, (c) fatigue F-0.23-c experiment.

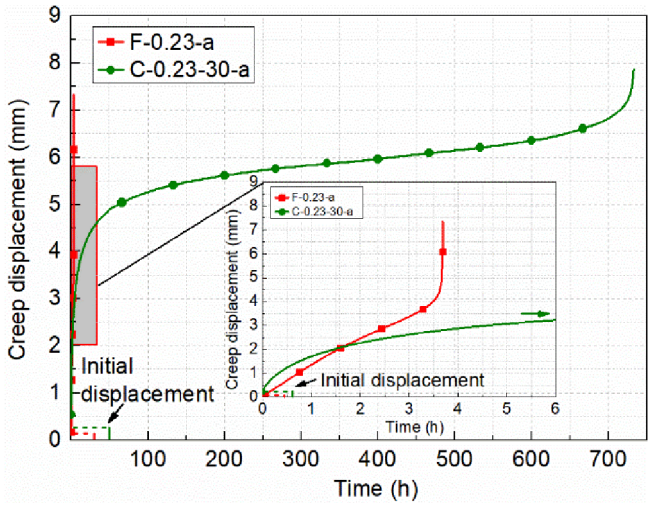

Fig. 31. Creep displacements of 1) creep experiment C-0.23-30-a, at 6.93 kN and 30 °C, and 2) fatigue experiment F-0.23-a, at 6.93 kN mean load and average temperature of 30 °C at stage 2.

high load levels, however, the effect of fatigue damage on creep displacements was greater than that of creep damage.

4.3. Fatigue/creep-temperature interaction

Significant temperature increases were observed at the third stage as failure approached. These increases were more significant at low load levels than at high load levels, see Fig. 27. Accumulated damage due to fatigue and creep was much more severe at low load levels, as confirmed by the total dissipated energy (TDE, Fig. 21), thus causing much more friction and associated heat generation.

The temperature increase also affected creep displacements and stiffness, i.e. accelerated creep (according to Fig. 14) and reduced stiffness (according to Fig. 7). The large drop of the cyclic stiffness to only about 20% at the lowest load levels during stage 3 (Fig. 23) may be explained by material softening due to the high temperature increase (Fig. 27). According to the DMA results, stiffness at these elevated temperatures decreased to very low values.

Since fatigue failure was dependent on the displacement and the latter was almost identical to the cyclic creep displacement (since the maximum difference, i.e. $d_{f,av}$ - $d_{f,\max,}$ was small, see definition in Fig. 19), failure in the fatigue experiments always occurred due to cyclic creep. Creep however was affected by different mechanisms. It was accelerated by 1) damage caused by fatigue, mainly at high load levels, 2) damage caused by creep in the tertiary stage, mainly at low load levels, and 3) temperature, mainly at low load levels towards the end of the fatigue life. At the low load levels, the slight temperature increase shown in Fig. 27 already at the beginning may also explain the stiffness decrease during the first stage, shown in Fig. 23.

5. Conclusions

An experimental investigation of the tension-tension fatigue behavior of ductile adhesively-bonded FRP joints was conducted. The ductility was provided by an acrylic adhesive in the rubbery state at ambient temperature. The mechanical degradation of the joints during the fatigue loading was characterized by the cyclic energy dissipation, cyclic stiffness, cyclic creep displacement and self-generated temperature variations. The effect of elevated temperatures on the static tensile and pure creep behaviors of the joints was also investigated. Based on these results, the fatigue-creep-temperature interactions were discussed and the following conclusions were derived:

(1) Although the ductile adhesive was in the rubbery state at ambient and elevated temperatures, it still exhibited considerable sensitivity to the loading rate and temperature. The static and creep responses significantly depended on temperature, with the exception of the failure displacements.
(2) Independent of the loading history (static, creep, fatigue, temperature loading), all joints failed in the adhesive layer at almost the same failure displacement. This behavior was associated with full stretching of the adhesive's molecular chains and subsequent failure of the primary bonds, which should be independent of the loading history. The full stretching was made possible by 1) the loss of the secondary bonds, either by yielding, creep or temperature, or 2) damage, caused by fatigue or creep. Cases of smaller failure displacements could be attributed to incomplete stretching, e.g. due to a higher loading rate or higher fatigue amplitude.
(3) During the fatigue loading, the cyclic energy dissipation, cyclic stiffness, cyclic creep displacements and self-generated temperature exhibited a basically similar three-stage behavior, showing an increase/decrease of the values in the first stage, a steady second stage with no or only small increases/decreases up to 80–90% of fatigue life, and a third stage with rapid increases/decreases, respectively, up to failure.
(4) Since the failure displacements under fatigue almost corresponded to the cyclic creep displacements, it was concluded that fatigue failure was driven by cyclic creep. These cyclic creep displacements were accelerated, at high load levels, mainly by damage caused by fatigue, and at low load levels, mainly by damage caused by creep in the tertiary stage and self-generated temperature towards the end of the fatigue life.

CRediT authorship contribution statement

Lulu Liu: Investigation, Formal analysis, Writing - original draft. **Xin Wang:** Validation, Review & editing, Funding acquisition. **Zhishen Wu:** Resources, Supervision. **Thomas Keller:** Conceptualization, Validation, Writing - review & editing, Supervision.

Declaration of Competing Interest

The authors declare that they have no known competing financial interests or personal relationships that could have appeared to influence the work reported in this paper.

Acknowledgements

The authors gratefully acknowledge the financial support provided by National Natural Science Foundation of China (No. 51878149); National Key Research and Development Program of China (No. 2017YFC0703000), China; Postgraduate Research and Innovation Plan of Jiangsu Province (No. KYCX18_0110), Jiangsu Province, China and China Scholarship Council (No. 201806090249), China. The authors also acknowledge Jiangsu GMV for providing the BFRP pultrusions and Sika AG for the adhesives.

Data availability statement

The raw/processed data required to reproduce these findings cannot be shared at this time as the data also forms part of an ongoing study.

References

[1] Bakis CE, Bank LC, Brown VL, Cosenza E, Davalos JF, Lesko JJ, et al. Fiber-reinforced polymer composites for construction—state-of-the-art review. J Compos Constr 2002;6(2):73–87. https://doi.org/10.1061/(ASCE)1090-0268(2002)6:2(73).
[2] Wu Z, Wang X, Zhao X, Noori M. State-of-the-art review of FRP composites for major construction with high performance and longevity. Int J Sustain Mater Struct Syst 2014;1:201. https://doi.org/10.1504/IJSMSS.2014.062757.
[3] Keller T, Bai Y, Vallée T. Long-term performance of a glass fiber-reinforced polymer truss bridge. J Compos Constr 2007;11:99–108. https://doi.org/10.1061/(ASCE)1090-0268(2007)11:1(99).
[4] CEN/TC 250. Design of fibre-polymer composite structures. Technical specification, final draft, prEN 19101; 2020.
[5] Vassilopoulos AP. In: Fatigue and fracture of adhesively-bonded composite joints behaviour, simulation and modelling. Elsevier, Woodhead; 2014. https://doi.org/10.1016/C2013-0-16372-6.
[6] Banea MD, da Silva LFM. Adhesively bonded joints in composite materials: an overview. Proc Inst Mech Eng Part L J Mater Des Appl 2009;223:1–18. https://doi.org/10.1243/14644207JMDA219.
[7] de Castro J, Keller T. Ductile double-lap joints from brittle GFRP laminates and ductile adhesives, Part I: Experimental investigation. Compos Part B Eng 2008;39:271–81. https://doi.org/10.1016/j.compositesb.2007.02.015.
[8] Angelidi M, Vassilopoulos AP, Keller T. Ductile adhesively-bonded timber joints – Part 1: Experimental investigation. Constr Build Mater 2018;179:692–703. https://doi.org/10.1016/j.conbuildmat.2018.05.214.
[9] Eslami G, Yanes-Armas S, Keller T. Energy dissipation in adhesive and bolted pultruded GFRP double-lap joints under cyclic loading. Compos Struct 2020;248:112496. https://doi.org/10.1016/j.compstruct.2020.112496.
[10] Liu L, Wang X, Wu Z, Keller T. Resistance and ductility of FRP composite hybrid joints. Compos Struct 2021;255:113001. https://doi.org/10.1016/j.compstruct.2020.113001.
[11] Abdel Wahab MM. Fatigue in adhesively bonded joints: a review. ISRN Mater Sci 2012;2012:1–25. https://doi.org/10.5402/2012/746308.
[12] Zuo P, Vassilopoulos AP. Review of fatigue of bulk structural adhesives and thick adhesive joints. Int Mater Rev 2020. https://doi.org/10.1080/09506608.2020.1845110.
[13] Crocombe AD, Richardson G. Assessing stress state and mean load effects on the fatigue response of adhesively bonded joints. Int J Adhes Adhes 1999;19:19–27. https://doi.org/10.1016/S0143-7496(98)00049-9.
[14] Sarfaraz R, Vassilopoulos AP, Keller T. Experimental investigation and modeling of mean load effect on fatigue behavior of adhesively-bonded pultruded GFRP joints. Int J Fatigue 2012;44:245–52. https://doi.org/10.1016/j.ijfatigue.2012.04.021.
[15] Olajide SO, Arhatari BD. Progress on interacting fatigue, creep & hysteretic heating in polymer adhesively bonded composite joints. Int J Fatigue 2017;98:68–80. https://doi.org/10.1016/j.ijfatigue.2017.01.021.
[16] Gomatam RR, Sancaktar E. The effects of stress state, loading frequency and cyclic waveforms on the fatigue behavior of silver-filled electronically-conductive adhesive joints. J Adhes Sci Technol 2006;20:53–68. https://doi.org/10.1163/156856106775212378.
[17] Harris JA, Fay PA. Fatigue life evaluation of structural adhesives for automative applications. Int J Adhes Adhes 1992;12:9–18. https://doi.org/10.1016/0143-7496(92)90003-F.
[18] Katunin A. Criticality of the self-heating effect in polymers and polymer matrix composites during fatigue, and their application in non-destructive testing. Polymers (Basel) 2018;11. https://doi.org/10.3390/polym11010019.
[19] Reis PNB, Monteiro JFR, Pereira AM, Ferreira JAM, Costa JDM. Fatigue behaviour of epoxy-steel single lap joints under variable frequency. Int J Adhes Adhes 2015;63:66–73. https://doi.org/10.1016/j.ijadhadh.2015.08.008.
[20] Movahedi-Rad AV, Keller T, Vassilopoulos AP. Fatigue damage in angle-ply GFRP laminates under tension-tension fatigue. Int J Fatigue 2018;109:60–9. https://doi.org/10.1016/j.ijfatigue.2017.12.015.
[21] Movahedi-Rad AV, Keller T, Vassilopoulos AP. Creep effects on tension-tension fatigue behavior of angle-ply GFRP composite laminates. Int J Fatigue 2019;123:144–56. https://doi.org/10.1016/j.ijfatigue.2019.02.010.
[22] Liu ZY, Beniwal S, Jenkins CHM, Winter RM. The coupled thermal and mechanical influence on a glassy thermoplastic polyamide: nylon 6, 6 under vibro-creep. Mech Time-Dependent Mater 2004;8:235–53. https://doi.org/10.1023/B:MTDM.0000046752.86686.cf.
[23] Saux V Le, Marco Y, Calloch S, Doudard C, Charrier P, Saux V Le, et al. Fast evaluation of the fatigue lifetime of elastomers based on a heat build-up protocol and micro-tomography measurements. Int J Fatigue 2010;32:1582–90. https://doi.org/10.1016/j.ijfatigue.2010.02.014.

[24] Ovalle Rodas C, Zaïri F, Naït-Abdelaziz M. A finite strain thermo-viscoelastic constitutive model to describe the self-heating in elastomeric materials during low-cycle fatigue. J Mech Phys Solids 2014;64:396–410. https://doi.org/10.1016/j.jmps.2013.10.010.
[25] Lee BL, Liu DS. Cumulative damage of fiber-reinforced elastomer composites under fatigue loading. J Compos Mater 1994;28:1261–86. https://doi.org/10.1177/002199839402801306.
[26] Eftekhari M, Fatemi A. Creep-fatigue interaction and thermo-mechanical fatigue behaviors of thermoplastics and their composites. Int J Fatigue 2016;91:136–48. https://doi.org/10.1016/j.ijfatigue.2016.05.031.
[27] Miyano Y, Nakada M, Yonemori T, Sihn S, Tsai SW. Time and temperature dependence of static, creep, and fatigue behavior for FRP adhesive joints. In: Proc, 12th Int Conf Compos Mater. p. 2–11.
[28] Mall S, Yun KT. Effect of adhesive ductility on cyclic debond mechanism in composite-to-composite bonded joints. J Adhes 1987;23:215–31. https://doi.org/10.1080/00218468708075408.
[29] Wang X, Zhao X, Wu Z, Zhu Z, Wang Z. Interlaminar shear behavior of basalt FRP and hybrid FRP laminates. J Compos Mater 2016;50:1073–84. https://doi.org/10.1177/0021998315587132.
[30] Wu G, Dong Z-Q, Wang X, Zhu Y, Wu Z-S. Prediction of long-term performance and durability of bfrp bars under the combined effect of sustained load and corrosive solutions. J Compos Constr 2015;19:04014058. https://doi.org/10.1061/(ASCE)CC.1943-5614.0000517.
[31] ASTM D3171-15. In: Standard test methods for constituent content of composite materials. ASTM Int; 2018. https://doi.org/10.1520/D3171-15.2.
[32] ASTM D3039/D3039M-17. In: Standard test method for tensile properties of polymer matrix composite materials. ASTM Int; 2017. https://doi.org/10.1520/D3039.
[33] Anon. SikaFast 5221 NT fast curing 2-C structural adhesive. Technical data sheet. Sika; 2005.
[34] Angelidi M, Keller T. Ductile adhesively-bonded timber joints – Part 2: strain rate effect. Constr Build Mater 2018;179:704–13. https://doi.org/10.1016/j.conbuildmat.2018.05.213.
[35] Angelidi M, Vassilopoulos AP, Keller T. Displacement rate and structural effects on Poisson ratio of a ductile structural adhesive in tension and compression. Int J Adhes Adhes 2017;78:13–22. https://doi.org/10.1016/j.ijadhadh.2017.06.008.
[36] ASTM D7028-07. In: Standard test method for glass transition temperature (DMA Tg) of polymer matrix composites by dynamic mechanical analysis (DMA). ASTM Int; 2017. https://doi.org/10.1520/D7028-07E01.2.
[37] Anon. Sikadur-330, 2-component epoxy impregnation resin. Technical data sheet. Sika; 2017.
[38] ASTM D2990-17. In: Standard test methods for tensile, compressive, and flexural creep and creep-rupture of plastics. ASTM Int; 2020. https://doi.org/10.1520/D2990-09.2.
[39] ASTM D3479/D3479M-16. In: Standard test method for tension-tension fatigue of polymer matrix composite. ASTM Int; 2020. https://doi.org/10.1520/D3479.
[40] ACI440 3R. In: Guide test methods for fiber-reinforced polymers (FRPs) for reinforcing or strengthening concrete structures. Am Concr Inst; 2004. p. 20–6.
[41] ASTM D5573-99. Standard practice for classifying failure modes in fiber-reinfoced plastic (FRP) joints. ASTM Int; 1999.
[42] Movahedi-Rad AV, Keller T, Vassilopoulos AP. Interrupted tension-tension fatigue behavior of angle-ply GFRP composite laminates. Int J Fatigue 2018;113:377–88. https://doi.org/10.1016/j.ijfatigue.2018.05.001.
[43] Cameselle-Molares A, Vassilopoulos AP, Keller T. Two-dimensional fatigue debonding in GFRP/balsa sandwich panels. Int J Fatigue 2019;125:72–84. https://doi.org/10.1016/j.ijfatigue.2019.03.032.